J Mater Sci (2020) 55:16323–16333

Energy materials

Porous carbon nanosheets derived from expanded graphite for supercapacitors and sodium-ion batteries

Chang Ma[1,2], Qingchao Fan[1], Mahmut Dirican[2], Yan Song[3], Xiangwu Zhang[2,*], and Jingli Shi[1,*]

[1] Tianjin Municipal Key Lab of Advanced Fiber and Energy Storage Technology, Tiangong University, Tianjin 300387, China
[2] Fiber and Polymer Science Program, Department of Textile Engineering, Chemistry and Science, Wilson College of Textiles, North Carolina State University, Raleigh, NC 27695-8301, USA
[3] CAS Key Laboratory of Carbon Materials, Institute of Coal Chemistry, Chinese Academy of Sciences, Taiyuan 030001, China

Received: 10 June 2020
Accepted: 21 August 2020
Published online: 2 September 2020

© Springer Science+Business Media, LLC, part of Springer Nature 2020

ABSTRACT

Two-dimensional carbons have attracted extensive interest in the field of energy storage and conversion owing to their unique nanostructure, high aspect ratios, and abundant surface-active sites. In this work, carbon nanosheets with developed porosity and high specific surface area were fabricated from expanded graphite (EG) by a siliconization/chlorination strategy. The worm-like macroporous structure and nanosheet morphology of EG are inherited by the resultant carbon nanosheet. The siliconization/chlorination strategy creates abundant micropores in EG, endowing the as-obtained carbon nanosheet with a high specific surface area of 1229 $m^2\ g^{-1}$ and a total pore volume of 0.75 $cm^3\ g^{-1}$. With high specific surface area, nanosheet morphology, and macroporous structure, the EG-based carbon nanosheet presents excellent performance when used as electrode materials of supercapacitors and sodium-ion batteries. When used as an electrode of supercapacitors, it delivers a specific capacitance of 210 F g^{-1}, retains 62% of the initial capacitance with increasing current density from 0.1 to 30 A g^{-1}, and maintains 98.6% of the initial capacitance after 5000 cycles. When used as the anode of sodium-ion batteries, it presents a reversible capacity of 198 mAh g^{-1} at 0.1 A g^{-1} and maintains 65 mAh g^{-1} after 1000 cycles at 5 A g^{-1}. The proposed strategy could be extended to other sp^2 carbon materials for a highly porous structure.

Handling Editor: Mark Bissett.

Address correspondence to E-mail: xiangwu_zhang@ncsu.edu; shijingli1963@163.com

https://doi.org/10.1007/s10853-020-05154-9

Introduction

Currently, the worldwide energy crisis and environmental pollution have been the primary issues that restrict the sustainable development of human society. It has come to a consensus for the importance and necessity to develop renewable clean energy. With the increasing exploitation of renewable energy and the popularization of portable electrics devices, much attention is focused on the high-efficiency and environment-friendly storage devices for electric power [1, 2], the most convenient and cleanest secondary energy. In the past several decades, electrochemical storage devices, including supercapacitors and batteries, have attracted widespread attention. A lot of efforts have been made in the development of advanced and cost-effective electroactive materials with unique structural characteristics.

Due to environmental friendliness, natural abundance, electrochemical durability, and high conductivity, carbon materials, especially carbon nanomaterials, have captured considerable attention. Up till now, various kinds of carbon nanomaterials, including zero-dimensional (0D) carbon black, fullerene and carbon dots, one-dimensional (1D) carbon nanotubes and nanofibers, two-dimensional (2D) carbon nanosheets, have been synthesized and investigated widely. Among them, carbon nanosheets have attracted great interest owing to unique properties, such as high aspect ratios, large lateral size, abundant and accessible active site, and high in-plane electrical conductivity [3–5]. Recently, porous carbon nanosheets (PCN) have been extensively researched as electrode materials of supercapacitors and secondary ion batteries, e.g., sodium-ion batteries [6, 7]. For example, Yanliang Wen et al. [8] have prepared a polystyrene-derived PCN via MgO-template method coupled with KOH activation, which was employed as the electrode of supercapacitors and showed capacitance of 135 F g^{-1}. Fei Sun et al. [9] have fabricated a PCN with a hierarchical porous structure using $Mg(OH)_2$ as template and coal tar as carbon precursor, showing a capacity of 113 mAh g^{-1} as anode of sodium-ion batteries.

Substantial work is focused on developing effective preparation routes to PCN with high qualities, such as high specific surface area (SSA), nanometer scale, and uniform structure. Graphene, the thinnest 2D carbon nanosheet with many amazing properties, has inspired a wave of research in the field of energy materials. However, graphene sheets tend to agglomerate or restack irreversibly due to strong van der Waals interactions, often leading to low SSA. Subsequently, researchers have fabricated porous graphene by selective etching of graphene, including KOH activation [10] and metal oxide nanoparticles etching [11]. Also, graphene has been used as a template to fabricate PCN by coating a porous carbon layer on it [3, 12, 13]. For instance, Ruili Liu et al. [14] have prepared graphene-templated porous carbon nanosheets by in situ growth of phenol–formaldehyde (PF) resin on graphene with triblock copolymer Pluronic F-127 as soft template, followed by carbonization. Besides the fabrication strategies based on graphene, a lot of novel routes have been developed to prepare PCN in recent years, for example, activation method based on biomass [15, 16] or synthesized thermosetting organic precursors [17, 18], organic molecules/salt blending pyrolysis [19, 20], hard templated method [21, 22], pyrolysis of 2-D precursors [23], self-assembly and pyrolysis technology [24–26], chemical blowing strategy [27, 28], and reduction of CO_2 [29]. Despite success in fabricating PCNs with a wide variety of unique structures, these strategies always involve one or more deficiencies, such as lengthy and complicated processes, costly raw materials, poor efficiency, unsatisfying carbon yield, limited SSA, and uneven microstructure or morphology. Hence, it is still of great significance to develop an efficient synthesis strategy for high-quality PCN to address the above-mentioned deficiencies.

Herein, expanded graphite (EG), a typical sp^2 carbon with unique nanosheet-like morphology, was transformed to PCN using a siliconization/chlorination strategy. EG was siliconized by Si vapor first, and then, the as-formed SiC was etched by chlorination, leaving porous carbon. A developed porous structure and high SSA of 1229 m^2 g^{-1} were achieved. The siliconization/chlorination operation was carried out in a simplified two-step process. The nanosheet morphology and macroporous structure of EG were inherited by the final PCN. It could be expected that the route can be extended to other carbons such as carbon nanotubes and multilayer graphene for making pores. To explore possible applications in energy storage devices, the resultant PCN was investigated as electrode materials of both supercapacitors and sodium-ion batteries.

Experimental

Reagents and chemicals

Silicon (~ 10 μm, 99.99%) was purchased from Fuzhou Hongjing Chemical Technology Co., Ltd. Expanded graphite (EG worm, 99.8%) was purchased from Qingdao Yanhai Carbon Materials Co., Ltd.

Preparation of expanded graphite-based PCN

PCN was synthesized with worm-like EG as precursor using a siliconization/chlorination strategy. Typically, 1.5 g of Si powder was placed in a porcelain boat, covered with 0.4 g of EG. The siliconization of EG was accomplished at 1500 °C for 2 h under an atmosphere of high purity argon. Subsequently, the furnace temperature was decreased to 800 °C and the argon atmosphere was shifted to chlorine atmosphere. The Si atoms were etched by chlorination at 800 °C for 3 h. The siliconization/chlorination process is presented schematically in Fig. 1 based on the following reactions:

$$C(s, EG) + Si(g) = SiC(s) \quad (1)$$

$$SiC(s) + 2Cl_2(g) = SiCl_4(g) + C(s, porous\ carbon) \quad (2)$$

The final EG-based PCN was labeled as EGPCN. The intermediate product before chlorination was also collected and named as EG-SiC. Photographs of the products at various stages are displayed in Fig. S1. Of particular note is that, in this process, $SiCl_4$ can be easily collected and recycled.

Characterizations

The morphology and microstructures of EG and EGPCN were characterized by scanning electron microscopy (SEM, Hitachi S4800, Japan) and transmission electron microscopy (TEM, JEM-2100, Japan). X-ray diffraction (XRD) patterns were collected by Bruker D8 diffractometer equipped with Cu-Kα radiation (λ = 0.15406 nm). The element composition and chemical bonding states of EGPCN were characterized by X-ray photoelectron spectroscopy (XPS, Thermo ESCALAB250, USA). The Raman spectra of EGPCN were recorded on Raman spectroscopy (Horiba XploRA, excited by a 638 nm laser). The SSA and porous texture of EG and EGPCN were investigated by N_2 adsorption/desorption measurement at 77 K on a physical adsorption apparatus (ASAP2020, Micromeritics). Pore volume was calculated from the adsorbed amount at a relative pressure P/P_0= 0.994. The SSA was calculated by the conventional Brunauer–Emmett–Teller (BET) method, and the pore size distribution was calculated using the NLDFT model.

Electrochemical measurements

The electrochemical performance of both EG and EGPCN as electrodes of supercapacitors was investigated using a three-electrode system with 6 M KOH

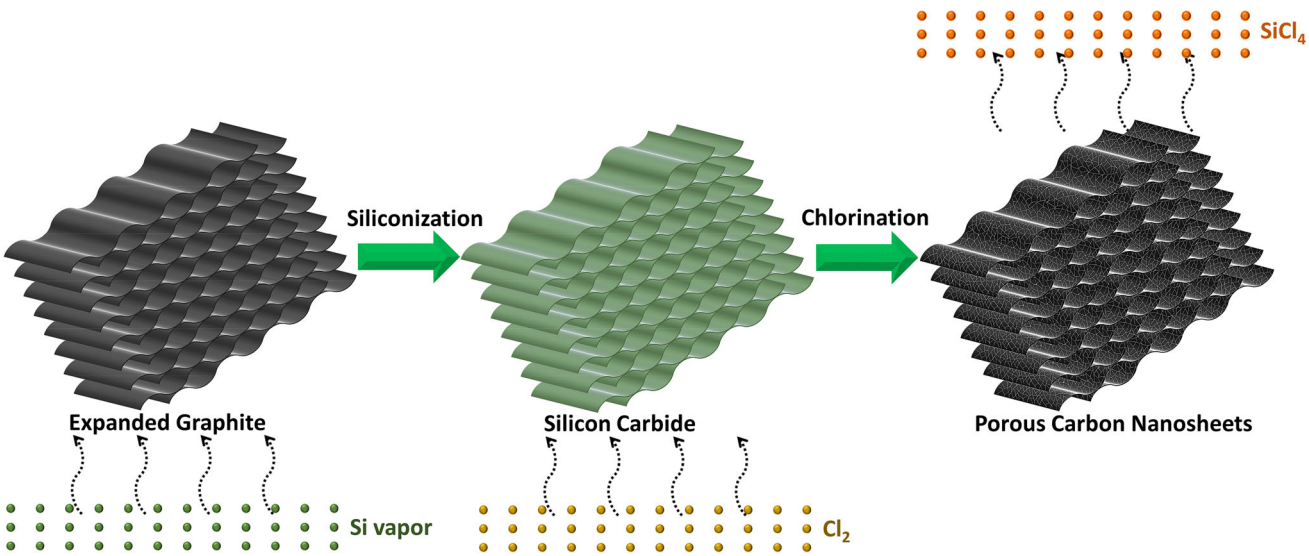

Figure 1 Schematic diagram of the preparation process from EG to PCNs.

as electrolyte, platinum as counter electrode and Hg/HgO as reference electrode. The working electrodes were fabricated by mixing active materials, acetylene black, and polytetrafluoroethylene with a weight ratio of 8: 1: 1 in ethanol. The electrodes were dried in vacuum at 120 °C for 12 h, and then cut and pressed onto circular nickel foam under a pressure of 10 MPa. The mass loading of active material on the dried working electrodes was 3.0–3.5 mg cm^{-2}. Before testing, the working electrodes were immersed in the electrolyte solution for 24 h to ensure complete wetting. All cyclic voltammetry (CV), galvanostatic charge/discharge (GCD), and electrochemical impedance spectroscopy (EIS) measurements were measured on a CHI760D electrochemical workstation (Shanghai Chenhua Apparatus Co. Ltd) at room temperature.

The sodium storage performance of both EG and EGPCN was evaluated using CR2430 coin-type cells with metal sodium as reference electrode and 1 M $NaClO_4$ in ethylene carbonate and dimethyl carbonate (EC: DEC, 1:1, v/v) with 5% fluoroethylene carbonate (v/v) as electrolyte. Working electrodes were fabricated by mixing 80 wt% of active materials, 10 wt% of acetylene black, and 10 wt% of polyvinylidene fluoride, which was then pasted on copper foil followed by drying under vacuum at 120 °C for 10 h. The mass loading of active material on each electrode is about 1.5–2.0 mg cm^{-2}. Cells were assembled in an argon-filled glove box, where water and oxygen concentration was kept less than 1 ppm. The GCD measurements were performed using a battery test system (CT2001A, LAND) with a cut-off voltage window of 0–2.5 V. CVs were recorded on the CHI760D electrochemical workstation.

Results and discussion

From SEM images of EG and EGPCN, shown in Fig. 2, it can be seen that EGPCN displays similar morphology to EG, including the worm-like macroporous structure and nanosheet morphology (Fig. S2). It demonstrates that the morphology of EG is well maintained during the siliconization/chlorination process, showing a similar shape memory effect to previous reports [30, 31]. The fluffy sample (Fig. S1) presents a complete color change from dark gray to light green, then to dark black. From the change in color, a rough judgment on the transformation degree can be made. To ensure a complete transformation from C to SiC, excessive Si was used. Without the introduction of oxygen, the transformation from C to SiC is believed to achieve based on reaction, Si + C = SiC, different from the shape memory synthesis, which is based on the gas–solid reaction between a vapor of SiO and C [31, 32]. There are no signs that liquid Si participates in the reactions with C. Larciprete et al. have revealed that Si atoms can be evaporated from Si substrate and react with C at temperature above 1127 °C [33]. As a consequence, it can be deduced that the formation of SiC is achieved through a gas–solid reaction, Si(g) + C(s) = SiC(s). EGPCN presents evident pores within the sheets, demonstrating that the chlorination etching is violent and leads to the formation of the porous sheets.

The XRD patterns of EG, EG-SiC, and EGPCN are demonstrated in Fig. 3. From the XRD pattern of EG, a strong diffraction peak with a lattice spacing of 0.3363 nm is observed, which can be attributed to the (002) peak of graphite. The precursor, EG, is of a highly crystal structure of sp^2 carbon. The XRD patterns of EG-SiC confirm a cubic crystal structure of SiC. Typical peaks located at 35.6°, 41.2°, 60.2°, 72.1°, and 75.5° can be ascribed to (111), (200), (220), (311), and (222) crystal planes of β-SiC, respectively. The transformation from EG to EG-SiC proves that Si atoms successfully diffuse into carbon and all the C atoms are chemically bonded with Si atoms. In the XRD pattern of EGPCN, two broad peaks at around 23° and 44° are observed, demonstrating a typical characteristic of amorphous carbons. It means all the Si atoms escape in the form of $SiCl_4$. Additionally, the Raman spectra of EGPCN (Fig. S3) show two broad bands at 1320 and 1585 cm^{-1}, corresponding to the D and G bands of carbon, respectively. The I_D/I_G intensity ratio is calculated to be 3.04, revealing the disordered structure of carbon again. No Si-related species were detected by XPS measurement (Fig. S4), also confirming no Si residue. These results demonstrate that EG with a high-order degree was transformed into a disordered carbon after siliconization/chlorination.

Figure 4 presents the HRTEM images of EG and EGPCN. It can be seen from Fig. 4a and d that both EG and EGPCN show typical 2D nanosheet morphology, confirming that the 2D morphology is maintained during the siliconization/chlorination process. Figure 4b, c, e, and f displays the TEM

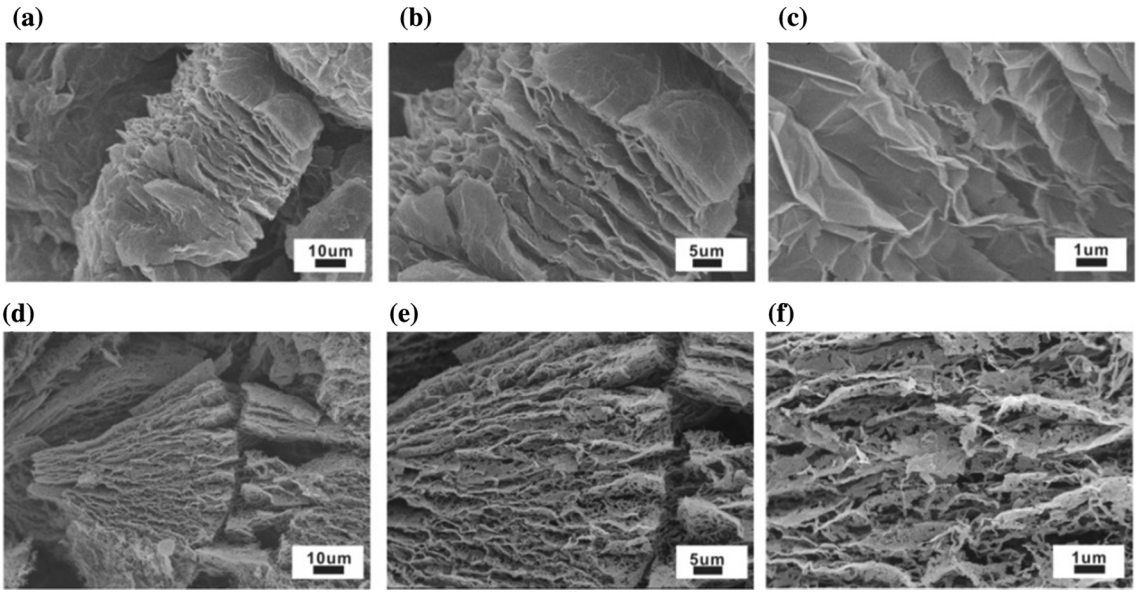

Figure 2 SEM images of EG (**a**, **b**, **c**) and EGPCN (**d**, **e**, **f**) with different magnifications.

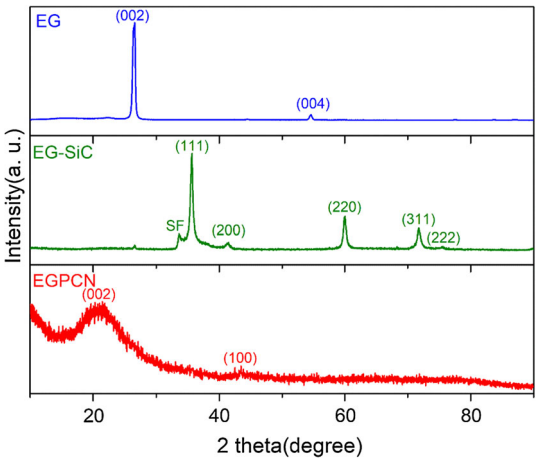

Figure 3 XRD patterns of EG, EG-SiC, and EGPCN.

images of EG and EGPCN at high amplification. EG exhibits a layered graphite structure, and the d_{002} is measured to be about 0.335 nm, close to the value calculated from the XRD pattern. EGPCN shows a disordered and highly nanoporous structure, indicating a successful transformation from sp^2 hybridized nonporous carbon to porous carbon. Considering that EG-SiC presents a typical crystal feature of β-SiC, of which d_{111} is 0.25 nm (Fig. 5S), the transformation reflects a violent etching of Si atoms and rearrangement of C atoms. Since the formation of carbide-derived carbon from SiC is known to be a conformal process [34], it is the extraction of Si atoms that brings about a large quantity of pores. And, during the process, rearrangement of C atoms prevents the formation of ordered pores, leaving pores distributed disorderedly.

The SSA and porous structure of EG and EGPCN were investigated using nitrogen physisorption measurements. From nitrogen sorption isotherms (Fig. 5a), significant adsorption takes place on EGPCN at the relative pressure below 0.1, while there is almost no uptake for EG. It implies that the atom etching produces considerable micropores. A remarkable vertical tail and hysteresis loop are observed at P/P_0 of 0.9–1.0 for both EG and EGPCN, confirming that EGPCN inherits a portion of mesopores and macropores of EG. It is consistent with the SEM observation that the worm-like porous structure is well preserved.

Figure 5b shows the pore size distribution of EG and EGPCN. EG has a small number of mesopores and macropores, while EGPCN presents abundant micropores in addition to a few mesopores and macropores. The micropores of EGPCN stem from the etching of Si atoms, while the mesopores and macropores are inherited from EG. EG shows a limited BET SSA of 54 $m^2\ g^{-1}$, a total pore volume of 0.21 $cm^3\ g^{-1,}$ and almost no micropores. After Si atom etching, EGPCN demonstrates a BET SSA of 1229 $m^2\ g^{-1}$, a total pore volume of 0.75 $cm^3\ g^{-1}$, and a microporosity of 64%. The achieved SSA is at the same level as those of reported SiC-derived carbons [35, 36], also reflecting the completeness of both two

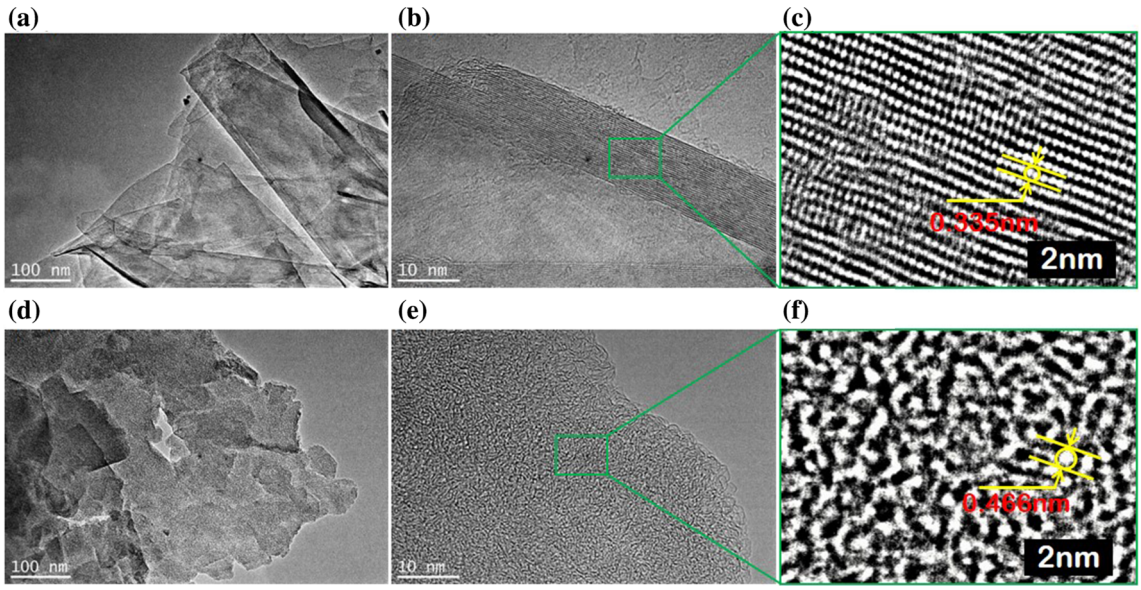

Figure 4 HRTEM images of EG (**a**, **b**, **c**) and EGPCN (**d**, **e**, **f**).

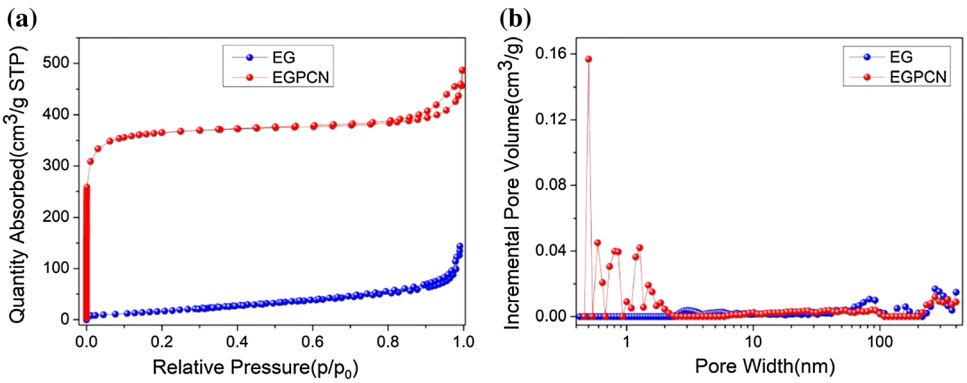

Figure 5 **a** Nitrogen adsorption–desorption isotherms. **b** Pore size distributions.

transformation processes. The siliconization/chlorination strategy introduces substantial pores in the sp^2 carbon while maintaining the initial morphology of carbon. It can be predicted that this strategy can be extended to other sp^2 carbon materials, e.g., carbon nanotube and multilayer graphene, for developing porous structure. In this sense, it possesses a distinct superiority in comparison with the activation method, which is hard to achieve a highly porous structure in the sp^2 carbons [37, 38]. Moreover, the pore-making in the process is based on the introduction and etching of foreign non-carbon atom, bringing about a high carbon yield of ~ 83%. It is greatly different from the activation method and metal oxides-etching approach [10, 11], both of which produce pores by etching C atoms and often result in a low carbon yield below 50% [39, 40].

To evaluate the electrochemical performance of EGPCN as electrode of supercapacitors, the CV and GCD measurements were carried out with 6M KOH solution as electrolyte. For comparison, EG was also tested under the same condition. Figure 6a presents the CV curves of both EGPCN and EG electrodes measured at scan rate of 5–100 mV s^{-1}. EGPCN shows a much higher specific capacitance than EG, of which the capacitance is almost negligible. EGPCN displays an apparent hump in the CV curves in the low potential range, indicating the existence of faradic redox reaction at the surface. It can be attributed to O- or/and Cl-containing species on the surface of EGPCN, which were measured to be 4.5 at.% (O) and 2.5 at.% (Cl) (Fig. S4). When the scan rate is increased to 100 mV s^{-1}, the CV curve maintains a quasi-rectangular shape with an I(C)/V slope close to 1, indicating low equivalent series resistance and excellent

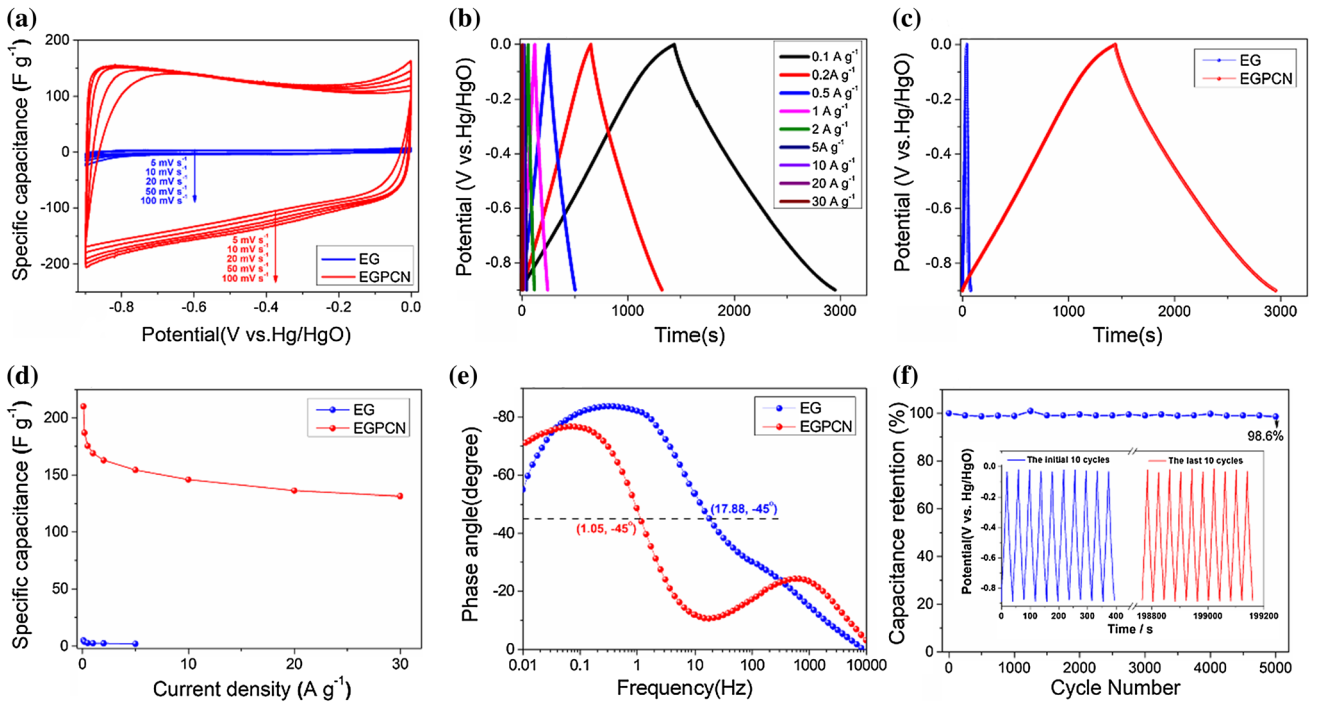

Figure 6 **a** CV curves for EG and EGPCN at different scan rates. **b** GCD curves of EGPCN at various current densities. **c** GCD curves at 0.1 A g^{-1}. **d** Specific capacitance at various current densities. **e** Frequency dispersion of the phase angle. **f** Change of the specific capacitance as a function of cycle number.

capacitive behavior. The GCD curves of EGPCN (Fig. 6b) are linear and shaped like isosceles triangular, revealing excellent electrochemical reversibility. The striking difference in the charge/discharge time (Fig. 6c) demonstrates a big boost in the specific capacitance for EGPCN. Based on the GCD tests, the specific capacitance of EG and EGPCN was calculated and plotted in Fig. 6d. At a current density of 0.1 A g^{-1}, the specific capacitance of EGPCN reaches 210 F g^{-1}, while that of EG is only 5 F g^{-1}. The significantly enhanced performance of EGPCN is attributed to its highly porous structure and considerable SSA. When current density was increased by 300 times, up to 30 A g^{-1}, the specific capacitance of EGPCN maintains 131 F g^{-1} with capacitance retention up to 62%, showing excellent high-rate performance. It is worth mentioning that EGPCN possesses much higher rate performance than most microporous carbons [41, 42]. It implies that a considerable proportion of surface is effectively utilized to form the electric double layer even in a limited current drain time. The nanometer scale of EGPCN plays a crucial role in accelerating ion response.

To gain insight into the kinetic behavior of both EG and EGPCN, EIS was performed in the frequency range from 0.01 Hz to 100 kHz. Figure 6e shows the dependence of phase angle with frequency of EG and EGPCN. The frequency for a phase angle of 45° marks the point at which the resistive and capacitive impedances are equal, which is defined as characteristic frequency f_0 [43]. In the phase angle-frequency curves, the f_0 value is found to be 1.05 Hz for EGPCN and 17.88 Hz for EG. The characteristic relaxation time constant τ_0 (= $1/f_0$, the minimum time needed to discharge all the energy from the device with an efficiency of greater than 50%) for both EG and EGPCN was also determined. With high conductivity, limited surface area, and ignorable porosity, EG shows an extremely low time constant (τ_0 = 0.056 s). Despite abundant micropores and high SSA, EGPCN presents a small time constant (τ_0 = 0.95 s), lower than those of activated carbons (5 s), carbon aerogels (2.38 s), hierarchical porous carbon (2.26 s), microporous nanofibers (1.56 s), and ordered mesoporous carbon (1.4 s) [44–47]. Additionally, the time constant of EGPCN is comparable to those of multiwalled carbon nanotubes (0.7 s) [48], highly graphitic hierarchical porous carbon (0.74 s) [49], porous carbon nanofibers (0.47–1.01 s) [50], and ordered mesoporous/microporous carbide-derived carbons

(0.62–0.92 s) [51]. Considering that ion transfer suffers from great resistance in micropores, the high-rate performance of EGPCN is mainly attributed to its nanosheet structure, which provides a short transfer passage for ions. Cycle life is another important requirement for supercapacitors. The cycling stability of EGPCN was evaluated by repeating the GCD test in 6 M KOH aqueous solution at current density of 5 A g^{-1}. The specific capacitance of EGPCN retains 98.6% of the 1st-cycle capacitance after 5000 cycles (Fig. 6f), indicating outstanding long-term electrochemical stability.

The energy storage performance of EGPCN and EG was also investigated using coin-type sodium-ion cells. Figure 7a shows CVs of EG and EGPCN electrodes at scan rate of 0.1 mV s^{-1}. For EGPCN, two cathodic peaks at ~ 0.48 and 1.07 V appear in the 1st discharge process, which become weaker and disappear in the subsequent cycles. For EG, a board cathodic peak ranging from 0.6 to 1.0 V emerges in the 1st cycle disappears in the 2nd cycle. This phenomenon is generally explained by the irreversible reactions between Na^+ and surface functional groups of electrode, electrolyte decomposition, and the formation of solid-electrolyte interphase (SEI) film on the electrode surface [52]. There is no cathodic peak located at around 0.01 V for both EG and EGPCN, signifying negligible Na^+ intercalation into graphite. The initial three GCD curves of EG and EGPCN recorded at current density of 0.1 A g^{-1} are presented in Fig. 7b and c, respectively. The first discharge and charge capacities are 930 and 198 mAh g^{-1} for EGPCN and 64 and 13 mAh g^{-1} for EG, both demonstrating a large irreversible capacity. It is associated with big SSA and surface functional groups [53]. No clear plateau region can be observed in the GCD curves of EG and EGPCN, consistent with the CV result that no cathodic peak appears at about 0.01 V. Based on these results, it is deduced that the energy storage is dominated by capacitive capacity, namely the adsorption of Na^+ on the defected sites, edges, and surface of carbon electrode. EGPCN delivers a considerable reversible capacity of 198 mAh g^{-1}, much higher than that of EG (13 mAh g^{-1}). The enhancement is attributed to the remarkably increased SSA, which plays a crucial role in forming the capacitive capacity. Figure 7d and e presents rate performance of EGPCN and EG at different current densities. At current density of 5 A g^{-1}, EGPCN retains a reversible specific capacity of 71 mAh g^{-1}, demonstrating a superior high-rate capacity to many porous carbons, including template mesoporous carbon (62 mAh g^{-1} at 5 A g^{-1}) [54], biomass-derived hierarchical porous carbons (47 mAh g^{-1} at 10 A g^{-1}) [55], graphene grids carbon(≈ 75 mAh g^{-1} at 0.28 A g^{-1}) [56], and nitrogen-rich mesoporous carbon (≈ 60 mAh g^{-1} at 5 A g^{-1}) [57]. When the current density was returned to 0.1 A g^{-1}, a reversible

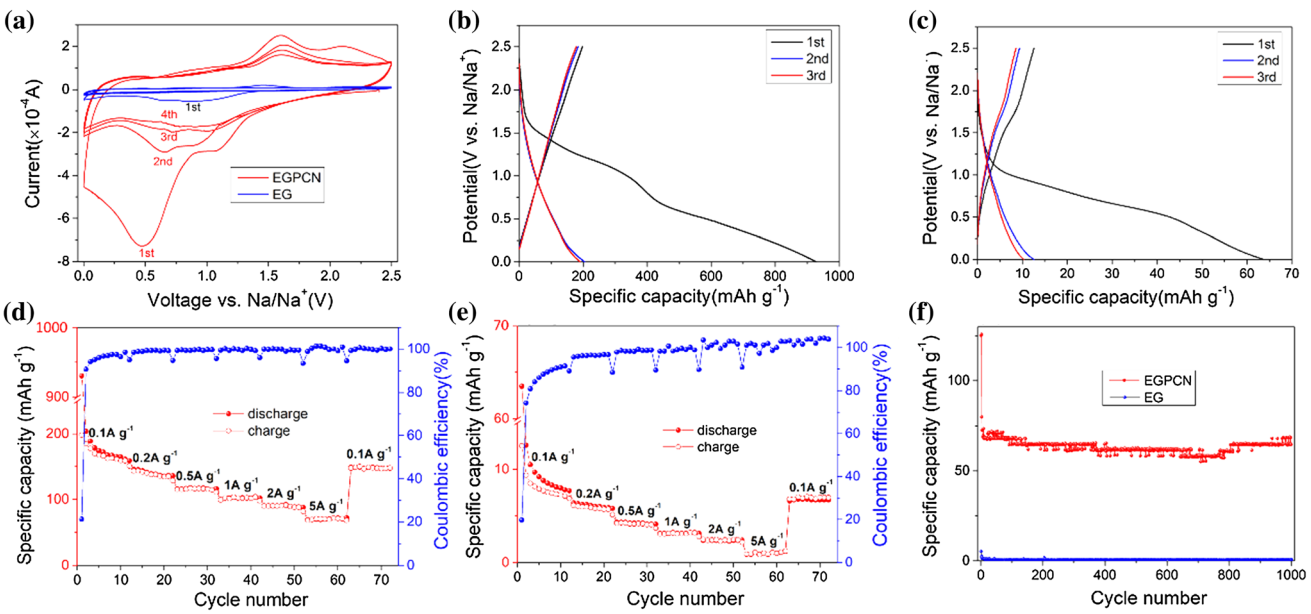

Figure 7 **a** CV curves of EGPCN and EG at 0.1 mV s^{-1}. **b**, **c** GCD curves of EGPCN and EG at 0.1 A g^{-1}. **d**, **e** Rate performance of EGPCN and EG at various current densities. **f** Cycling performance of EGPCN at 5 A g^{-1}.

capacity of 149 mAh g^{-1} was recovered. Compared with the capacity of the 10th cycle at 0.1 A g^{-1} (160 mAh g^{-1}), the capacity retention is calculated to be 93%, which is higher than those of most nanoporous carbons [58–60] and hard carbons [61, 62]. The considerable reversible capacity and rate performance are attributed to the unique worm-like porous structure and nanosheet morphology, which not only provide abundant surface-active sites for sodium-ion storage, ensure satisfactory structural stability, but also shorten sodium-ion diffusion pathway. Figure 7f shows the long-term cycling performance of EG and EGPCN at current density of 5 A g^{-1}. After activation for 3 cycles, the capacity is stabilized at 73 mAh g^{-1}. After 1000 cycles, the capacity maintains at 65 mAh g^{-1} with a retention rate of 89.1%, showing a superior cycling stability.

Conclusions

In summary, the siliconization/chlorination strategy can transform expanded graphite (EG) into porous carbon nanosheets (PCN). During the transformation process, the nanosheet morphology and worm-like macroporous structure of EG can be well preserved. The strategy can endow EG with developed micropores and high SSA. The EG-based PCN (EGPCN) possessed considerable SSA (1229 m^2 g^{-1}) and high microporosity (64%) for ion adsorption, and unique nanosheet morphology and macroporous structure for electron conduction and ion transport. Used as an electrode material for supercapacitors, EGPCN delivered a capacitance of 210 F g^{-1}, retained 62% of the initial capacitance with increasing current density from 0.1 to 30 A g^{-1}, and maintains 98.6% of the 1st-cycle capacitance after 5000 cycles. When used in sodium-ion batteries, it presented a reversible capacity of 198 mAh g^{-1} at 0.1 A g^{-1} and maintained 65 mAh g^{-1} after 1000 cycles at 5 A g^{-1}. The achieved EGPCN could be a potential candidate as electrode material for supercapacitors and sodium-ion batteries. Besides, the proposed strategy for preparing EGPCN could be extended to other sp^2 carbon materials and become a universal pore-making route for carbon.

Acknowledgements

This work was supported by Science & Technology Development Fund of Tianjin Education Commission for Higher Education (2017KJ072), National Nature Science Foundation of China (No. 51502201, U1510134), Natural Science Foundation of Tianjin Province (No. 16JCQNJC06300), and the China Scholarship Council (No. 201908120023).

Electronic supplementary material: The online version of this article (https://doi.org/10.1007/s10853-020-05154-9) contains supplementary material, which is available to authorized users.

References

[1] Wang D, Nai J, Li H, Xu L, Wang Y (2019) A robust strategy for the general synthesis of hierarchical carbons constructed by nanosheets and their application in high performance supercapacitor in ionic liquid electrolyte. Carbon 141:40–49

[2] Sun Y, Yu Z, Li T, Chen Y, Xia X (2019) Cryo-treatment in enhancing the electrochemical properties of SnSb/C nanofiber anodes for lithium ion batteries. Electrochim Acta 296:637–643

[3] Yuan K, Hu T, Xu Y et al (2016) Engineering the morphology of carbon materials: 2D porous carbon nanosheets for high-performance supercapacitors. ChemElectroChem 3:822–828

[4] Chen P, Wang L-K, Wang G, Gao M-R, Yu S-H (2014) Nitrogen-doped nanoporous carbon nanosheets derived from plant biomass: an efficient catalyst for oxygen reduction reaction. Energy Environ Sci 7:4095–4103

[5] H-g Wang ZWu, Meng F-l et al (2013) Nitrogen-doped porous carbon nanosheets as low-cost, high-performance anode material for sodium-ion batteries. Chemsuschem 6:56–60

[6] He Y, Zhuang X, Lei C et al (2019) Porous carbon nanosheets: synthetic strategies and electrochemical energy related applications. Nano Today 24:103–119

[7] Li F, Zhou Z (2018) Micro/nanostructured materials for sodium ion batteries and capacitors. Small 14:1702961

[8] Wen Y, Wen X, Wenelska K, Chen X, Mijowska E (2019) Novel strategy for preparation of highly porous carbon sheets derived from polystyrene for supercapacitors. Diamond Relat Mater 95:5–13

[9] Sun F, Wang K, Wang L et al (2019) Hierarchical porous carbon sheets with compressed framework and optimized pore configuration for high-rate and long-term sodium and lithium ions storage. Carbon 155:166–175

[10] Zhu Y, Murali S, Stoller MD et al (2011) Carbon-based supercapacitors produced by activation of graphene. Science 332:1537–1541

[11] Zhang X, Zhou J, Liu C, Chen X, Song H (2016) A universal strategy to prepare porous graphene films: binder-free anodes for high-rate lithium-ion and sodium-ion batteries. J Mater Chem A 4:8837–8843

[12] Hao G-P, Jin Z-Y, Sun Q, Zhang X-Q, Zhang J-T, Lu A-H (2013) Porous carbon nanosheets with precisely tunable thickness and selective CO_2 adsorption properties. Energy Environ Sci 6:3740–3747

[13] Wang Q, Yan J, Fan Z (2014) Nitrogen-doped sandwich-like porous carbon nanosheets for high volumetric performance supercapacitors. Electrochim Acta 146:548–555

[14] Liu R, Pan L, Liu X, Wu D (2015) An evaporation-induced tri-constituent assembly approach to fabricate an ordered mesoporous carbon/graphene aerogel for high-performance supercapacitors. RSC Adv 5:16765–16768

[15] Mondal AK, Kretschmer K, Zhao Y et al (2017) Nitrogen-doped porous carbon nanosheets from eco-friendly eucalyptus leaves as high performance electrode materials for supercapacitors and lithium ion batteries. Chem Eur J 23:3683–3690

[16] Hou J, Jiang K, Tahir M et al (2017) Tunable porous structure of carbon nanosheets derived from puffed rice for high energy density supercapacitors. J Power Sources 371:148–155

[17] Deng W, Zhang Y, Yang L, Tan Y, Ma M, Xie Q (2015) Sulfur-doped porous carbon nanosheets as an advanced electrode material for supercapacitors. RSC Adv 5:13046–13051

[18] Pachfule P, Shinde D, Majumder M, Xu Q (2016) Fabrication of carbon nanorods and graphene nanoribbons from a metal–organic framework. Nat Chem 8:718–724

[19] Liu B, Yang M, Chen H, Liu Y, Yang D, Li H (2018) Graphene-like porous carbon nanosheets derived from salvia splendens for high-rate performance supercapacitors. J Power Sources 397:1–10

[20] Cai C, Sui Q, She Z et al (2018) Two dimensional holey carbon nanosheets assisted by calcium acetate for high performance supercapacitor. Electrochim Acta 283:904–913

[21] Jayaramulu K, Dubal DP, Nagar B et al (2018) Ultrathin hierarchical porous carbon nanosheets for high-performance supercapacitors and redox electrolyte energy storage. Adv Mater 30:1705789

[22] Fang Y, Lv Y, Che R et al (2013) Two-Dimensional Mesoporous Carbon Nanosheets and Their Derived Graphene Nanosheets: synthesis and Efficient Lithium Ion Storage. J Am Chem Soc 135:1524–1530

[23] Zhao K, Liu S, Ye G, Gan Q, Zhou Z, He Z (2018) High-yield bottom-up synthesis of 2D metal–organic frameworks and their derived ultrathin carbon nanosheets for energy storage. J Mater Chem A 6:2166–2175

[24] Liu S, Wang F, Dong R et al (2016) Dual-template synthesis of 2D mesoporous polypyrrole nanosheets with controlled pore size. Adv Mater 28:8365–8370

[25] Xu Z, Zhuang X, Yang C et al (2016) Nitrogen-doped porous carbon superstructures derived from hierarchical assembly of polyimide nanosheets. Adv Mater 28:1981–1987

[26] Yang J, Zhou X, Wu D, Zhao X, Zhou Z (2017) S-doped N-rich carbon nanosheets with expanded interlayer distance as anode materials for sodium-ion batteries. Adv Mater 29:1604108

[27] Wang X, Zhang Y, Zhi C et al (2013) Three-dimensional strutted graphene grown by substrate-free sugar blowing for high-power-density supercapacitors. Nat Commun 4:2905

[28] Chang B, Yin H, Zhang X, Zhang S, Yang B (2017) Chemical blowing strategy synthesis of nitrogen-rich porous graphitized carbon nanosheets: morphology, pore structure and supercapacitor application. Chem Eng J 312:191–203

[29] Wang J, Chen S, Deng H, Tang S, Cao Y-C, Liang J (2019) Simple synthesis of porous carbon sheet by reduction reaction of in situ formed carbon dioxide for supercapacitor application. Results Phys 12:1340–1343

[30] Liu Z, Ci L, Jin-Phillipp NY, Rühle M (2007) Vapor–solid reaction for silicon carbide hollow spherical nanocrystals. J Phys Chem C 111:12517–12521

[31] Pham-Huu C, Keller N, Ehret G, Ledoux MJ (2001) The First Preparation of Silicon Carbide Nanotubes by Shape Memory Synthesis and Their Catalytic Potential. J Catal 200:400–410

[32] Pan Z, Lai H-L, Au FCK et al (2000) Oriented silicon carbide nanowires: synthesis and field emission properties. Adv Mater 12:1186–1190

[33] Larciprete R, Lizzit S, Cepek C, Botti S, Goldoni A (2003) Thermal reactions at the interface between Si and C nanoparticles: nanotube self-assembling and transformation into SiC. Surf Sci 532–535:886–891

[34] Cambaz ZG, Yushin GN, Gogotsi Y, Vyshnyakova KL, Pereselentseva LN (2006) Formation of carbide-derived carbon on beta-silicon carbide whiskers. J Am Ceram Soc 89:509–514

[35] Kormann M, Gerhard H, Popovska N (2009) Comparative study of carbide-derived carbons obtained from biomorphic TiC and SiC structures. Carbon 47:242–250

[36] Korenblit Y, Rose M, Kockrick E et al (2010) High-rate electrochemical capacitors based on ordered mesoporous silicon carbide-derived carbon. ACS Nano 4:1337–1344

[37] Barzegar F, Bello A, Momodu D, Madito MJ, Dangbegnon J, Manyala N (2016) Preparation and characterization of porous carbon from expanded graphite for high energy density supercapacitor in aqueous electrolyte. J Power Sources 309:245–253

[38] Ka BH, Oh SM (2008) Electrochemical activation of expanded graphite electrode for electrochemical capacitor. J Electrochem Soc 155:A685–A692

[39] Maciá-Agulló JA, Moore BC, Cazorla-Amorós D, Linares-Solano A (2004) Activation of coal tar pitch carbon fibres: physical activation vs. chemical activation. Carbon 42:1367–1370

[40] Wang J, Kaskel S (2012) KOH activation of carbon-based materials for energy storage. J Mater Chem 22:23710–23725

[41] Dong X-L, Lu A-H, He B, Li W-C (2016) Highly microporous carbons derived from a complex of glutamic acid and zinc chloride for use in supercapacitors. J Power Sources 327:535–542

[42] Yun YS, Cho SY, Shim J et al (2013) Microporous carbon nanoplates from regenerated silk proteins for supercapacitors. Adv Mater 25:1993–1998

[43] Taberna PL, Simon P, Fauvarque JF (2003) Electrochemical characteristics and impedance spectroscopy studies of carbon–carbon supercapacitors. J Electrochem Soc 150:A292–A300

[44] Lewandowski A, Zajder M, Frąckowiak E, Béguin F (2001) Supercapacitor based on activated carbon and polyethylene oxide–KOH–H2O polymer electrolyte. Electrochim Acta 46:2777–2780

[45] Liu Z, Fu D, Liu F et al (2014) Mesoporous carbon nanofibers with large cage-like pores activated by tin dioxide and their use in supercapacitor and catalyst support. Carbon 70:295–307

[46] Guo J, Wu D, Wang T, Ma Y (2019) P-doped hierarchical porous carbon aerogels derived from phenolic resins for high performance supercapacitor. Appl Surf Sci 475:56–66

[47] Sun K, Yu S, Hu Z et al (2017) Oxygen-containing hierarchically porous carbon materials derived from wild jujube pit for high-performance supercapacitor. Electrochim Acta 231:417–428

[48] Portet C, Yushin G, Gogotsi Y (2007) Electrochemical performance of carbon onions, nanodiamonds, carbon black and multiwalled nanotubes in electrical double layer capacitors. Carbon 45:2511–2518

[49] Ni L, Wang R, Wang H et al (2018) Designing nanographitic domains in N-doped porous carbon foam for high performance supercapacitors. Carbon 139:1152–1159

[50] Ma C, Song Y, Shi J et al (2013) Preparation and one-step activation of microporous carbon nanofibers for use as supercapacitor electrodes. Carbon 51:290–300

[51] Wu C, Gao J, Zhao Q et al (2014) Preparation and supercapacitive behaviors of the ordered mesoporous/microporous chromium carbide-derived carbons. J Power Sources 269:818–824

[52] Hou H, Banks CE, Jing M, Zhang Y, Ji X (2015) Carbon quantum dots and their derivative 3D porous carbon frameworks for sodium-ion batteries with ultralong cycle life. Adv Mater 27:7861–7866

[53] Tang K, Fu L, White RJ et al (2012) Hollow carbon nanospheres with superior rate capability for sodium-based batteries. Adv Energy Mater 2:873–877

[54] Cao B, Liu H, Xu B, Lei Y, Chen X, Song H (2016) Mesoporous soft carbon as an anode material for sodium ion batteries with superior rate and cycling performance. J Mater Chem A 4:6472–6478

[55] Wang H, Yu W, Shi J, Mao N, Chen S, Liu W (2016) Biomass derived hierarchical porous carbons as high-performance anodes for sodium-ion batteries. Electrochim Acta 188:103–110

[56] Zhang H, Guo HN, Li AY et al (2019) High specific surface area porous graphene grids carbon as anode materials for sodium ion batteries. J Energy Chem 31:159–166

[57] Liu H, Jia M, Yue S et al (2017) Creative utilization of natural nanocomposites: nitrogen-rich mesoporous carbon for a high-performance sodium ion battery. J Mater Chem A 5:9572–9579

[58] Wang X, Li G, Hassan FM et al (2015) Sulfur covalently bonded graphene with large capacity and high rate for high-performance sodium-ion batteries anodes. Nano Energy 15:746–754

[59] Luo X-F, Yang C-H, Peng Y-Y et al (2015) Graphene nanosheets, carbon nanotubes, graphite, and activated carbon as anode materials for sodium-ion batteries. J Mater Chem A 3:10320–10326

[60] Yang G, Song H, Cui H, Wang C (2015) Honeycomb in honeycomb carbon bubbles: excellent Li- and Na-storage performances. J Mater Chem A 3:20065–20072

[61] Bommier C, Luo W, Gao W-Y, Greaney A, Ma S, Ji X (2014) Predicting capacity of hard carbon anodes in sodium-ion batteries using porosity measurements. Carbon 76:165–174

[62] Lu P, Sun Y, Xiang H, Liang X, Yu Y (2018) 3D amorphous carbon with controlled porous and disordered structures as a high-rate anode material for sodium-ion batteries. Adv Energy Mater 8:1702434

Publisher's Note Springer Nature remains neutral with regard to jurisdictional claims in published maps and institutional affiliations.